# Spin current and spin transfer torque in ferromagnet/superconductor spin valves

Evan Moen* and Oriol T. Valls†
*School of Physics and Astronomy, University of Minnesota, 116 Church Street SE, Minneapolis, Minnesota 55455, USA*

(Received 9 February 2018; published 4 May 2018)

Using fully self-consistent methods, we study spin transport in fabricable spin valve systems consisting of two magnetic layers, a superconducting layer, and a spacer normal layer between the ferromagnets. Our methods ensure that the proper relations between spin current gradients and spin transfer torques are satisfied. We present results as a function of geometrical parameters, interfacial barrier values, misalignment angle between the ferromagnets, and bias voltage. Our main results are for the spin current and spin accumulation as functions of position within the spin valve structure. We see precession of the spin current about the exchange fields within the ferromagnets, and penetration of the spin current into the superconductor for biases greater than the critical bias, defined in the text. The spin accumulation exhibits oscillating behavior in the normal metal, with a strong dependence on the physical parameters both as to the structure and formation of the peaks. We also study the bias dependence of the spatially averaged spin transfer torque and spin accumulation. We examine the critical-bias effect of these quantities, and their dependence on the physical parameters. Our results are predictive of the outcome of future experiments, as they take into account imperfect interfaces and a realistic geometry.

DOI: 10.1103/PhysRevB.97.174506

## I. INTRODUCTION

Spintronic devices, such as spin valves, have seen increasing attention over the years due [1] to their expected technological applications (for example, to nonvolatile memory) and for their intrinsic scientific interest. Traditional spin valves [1] are composed of two ferromagnets ($F$) in close proximity, often separated by a normal metal or insulator. A charge current interacts with the exchange field of the first ferromagnetic component, inducing a polarization in its spin degree of freedom. The second $F$ component is introduced as a spin selector and detector, in which a spin current and spin accumulation are predicted and measured [2,3]. The charge current and the relative orientation of the exchange fields of the two ferromagnets determine the spin transport properties of these devices. In their application to nonvolatile memory, the magnetic memory is current-switched (as opposed to magnetic-field-switched) via the spin transfer torque (STT) [4–6]. This gives the devices an advantage in power consumption and scalability [7].

Superconducting spin valves are different. They are spintronic devices that include, in addition to the $F$ components, one or more layers of a superconducting ($S$) material. Thus, superconducting as well as ferromagnetic and normal components are involved. They are exciting, developing spintronic structures presenting their own unique set of properties and applications [8]. In these devices the presence of (usually traditional, well-understood) superconductors in proximity to ferromagnetic materials fundamentally affects spin transport. Furthermore, their ultralow power consumption offers a distinct advantage over standard spin valves, particularly in memory applications. Many such devices have been proposed [9–11]. The first spin switch device using a superconducting current was reported in Ref. [12]. Other superconducting spin valves with $F_1/N/F_2/S$ layered structures have since been studied [13–15]. The currents in such devices are in general spin-polarized and can potentially be controlled by STT in nanoscale devices, just as in traditional spin valves. However, they are not merely regular spin valves with spin currents. Rather, these are novel structures with their own distinct set of spin transport properties due to the $F/S$ proximity effects [16]. Below, we discuss some of the peculiar properties of these devices as they are relevant to our study.

Superconductivity results from the formation of Cooper pairs consisting of opposite-momentum electrons [17]. In the usual $s$-wave superconductivity, these pairs form a singlet state. Ferromagnetism, on the other hand, has a strong tendency to break these singlet pairs, while favoring in principle triplet pairing states with $m_z = \pm 1$. It would seem that ferromagnetism and $s$-wave superconductivity are largely incompatible. Indeed, the ordinary superconducting proximity effects in $F/S$ heterostructures result in a heavily damped, oscillatory behavior of the singlet pair amplitudes in the $F$-layer regions [18,19], caused by Cooper pairs acquiring a center-of-mass momentum [20]. This oscillatory behavior is critical to understanding $F/S$ heterostructures, as it makes all transport measurements highly dependent on the thicknesses of each material layer. However, proximity effects in $F/S$ structures are by no means limited to those arising from the $s$-wave Cooper pairs in the $S$ material. Indeed, there are long-range proximity effects from triplet pair correlations that are induced in the structure by the presence of nonuniform exchange fields [21–25]. This conversion is possible because, unless all exchange fields are collinear, the Hamiltonian does not commute with $S_z$, the $z$ component of the Cooper pair spins: thus it is not conserved.

*moenx359@umn.edu
†Also at Minnesota Supercomputer Institute, University of Minnesota, Minneapolis, Minnesota 55455, USA; otvalls@umn.edu

 

Because of the Pauli principle, the triplet correlations for a spatially even Cooper pair configuration must be odd in frequency [26] or equivalently in time [23]. In the presence of a uniform exchange field, only the $m_z = 0$ triplet component may be induced. The required nonuniform exchange field can be introduced in a variety of ways: for example one can have an $F_1/F_2/S$ heterostructure with noncollinear exchange fields, or a single $F$ layer with a nonuniform magnetization texture such as one may have with magnetic domains or, in a more controllable way, by using a magnet such as holmium [27–30] in which the magnetic structure is spiral. In these cases the presence of $m_z = \pm 1$ pairs is compatible with conservation laws and the Pauli principle, and in fact such pairs are usually induced. The exchange fields do not necessarily break these triplet correlations, and thus the proximity effect can be long-ranged [31–37] in $F$. In heterostructures which include two ferromagnetic layers $F_1$ and $F_2$, as we consider in this paper, one can immediately see that there will be an interesting angular dependence of the results on the misalignment angle $\phi$ between the two $F$ layers, as their orientations vary from being parallel, to orthogonal, to antiparallel. In traditional spin valves, this angular dependence is characterized by the magnetoresistance obtained by comparing the parallel (P) and antiparallel (AP) configurations [38]. In the superconducting devices, as triplet pairs are induced, singlet pair amplitudes decrease, diminishing the strength of the superconducting pair potential and influencing the transport properties [14,39]. As $\phi$ is varied between $0^\circ$ and $180^\circ$ a unique angular dependence that is nonmonotonic is produced.

The superconducting proximity effects discussed above affect both the thermodynamic and the transport properties of the device. A fundamental contribution to both arises from Andreev reflection [40] at the interfaces. Andreev reflection is the process of electron-to-hole conversion by the creation or annihilation of a Cooper pair, occurring at the interface of a superconductor. There are two types of Andreev reflection: conventional and anomalous. In conventional Andreev reflection, the reflected electron/hole has spin opposite to that of the incident particle. In anomalous Andreev reflection, these electron/hole pairs have the same spin. It has been shown [14,41–44] that normal and anomalous Andreev reflection are correlated with triplet proximity effects. Understanding and accurately characterizing the transmission amplitudes of the Andreev reflections is pertinent to all transport calculations in superconducting heterostructures [45–48], particularly for quantities with spatial dependence such as the spin current and spin transfer torque.

The practical fabrication of $F/F/S$ valve structures results in devices that deviate very significantly from theoretical idealizations. To be able to modify the angle $\phi$ requires the insertion of a normal metal spacer between the $F$ layers, so that they are decoupled and the magnetization of one of them can be rotated individually. In addition, even high-quality interfaces between all layers involved are not perfect: some interfacial scattering is inevitable and transport [10] in superconducting spin valves is very sensitive to it [39,48], as is also the case [49] for spin transport in traditional spin valves. It has been shown that if the the normal spacer and the interfacial scattering are properly taken into account, then it is possible to quantitatively characterize to high accuracy [50] the thermodynamic properties of high-quality devices. In recent work [39], we have also examined the charge transport properties of $F_1/N/F_2/S$ heterostructures with an emphasis on practical, realistic layer thicknesses and interfacial scattering parameters. However, spin transport properties, such as spin current and the STT, were calculated only for the "proof of principle" ideal case with no normal metal spacer or interfacial scattering parameters.

Developments in deposition techniques have allowed for the fabrication of spintronic devices [10] that can be described via clean limit methods. These are the high-quality devices [50] which are our focus in this paper. Thus, we assume geometrical (thickness of the layers, including that of $N$) and material parameters appropriate to the Co, Cu, and Nb layers used there [50]. The charge and spin transport properties depend strongly on the applied bias voltage. Many of their features [14,39] change rather abruptly when the applied voltage reaches the critical-bias (CB) value, which is related to the self-consistent pair potential within the superconductor. This value is less than the pair potential bulk value due to the proximity effects. The transport properties are quite different for an applied voltage bias below and above the CB. This effect is also dependent on the misalignment angle of the exchange fields, usually in a nonmonotonic [39] way. Here, we examine the dependence of the spin transport properties on the layer thicknesses, the importance of which has been mentioned above, the interfacial scattering strengths, and the applied bias voltage, including CB effects. We hope to establish a broad understanding of how sample quality and geometry affect spin transport results in $F_1/N/F_2/S$ systems so that they may then be compared to experimental results.

In our calculations, we use a self-consistent solution to the Bogoliubov–de Gennes (BdG) equations [51] to calculate the pair potential, and then employ this potential in the transport calculations via a transfer matrix method [39]. This method correctly incorporates the normal and Andreev reflection and transmission amplitudes of the electrons and holes. We evaluate then the spin current, the STT, and the magnetization, all as functions of position within the $F_1/N/F_2/S$ heterostructure and of the applied bias. We examine their dependence on the misalignment angle $\phi$. We also vary the layer thickness and the interfacial scattering strengths within bounds similar to those used in the study of the thermodynamic properties of similar systems [50]. Our focus will be the analysis of the physical parameters for experimental use, as well as on the underlying physics of the spin transport.

Spin transport is considerably more complex than charge transport. As opposed to the charge current, which is a constant through the sample due to charge conservation, the spin current varies with position, and this variation is related to the STT. Furthermore, since spin is a vector the spin current is in principle a tensor, although it does reduce to a vector in spin space in the quasi-one-dimensional geometry we will consider here. Thus all quantities are spatially dependent. Together with the spatially oscillatory nature of the singlet and triplet amplitudes, we find a strong and intricate dependence of spin transport on the layer thicknesses. Furthermore, the proximity effects are particularly influential on the spin transport properties, as they relate to the spin pairing and the induced triplets. We thus see a nonmonotonic dependence on $\phi$, as well as a strong

dependence on the interfacial scattering strengths. Interfacial scattering generally inhibits the proximity effects but, because there are several barriers, resonance features such as those found for charge transport [39] can also arise. We will also analyze the average of the spin transport quantities over each layer: we have found this particularly useful in studying the bias dependencies and in better establishing the underlying physical principles at work. We hope through this work to provide future experiments with some deeper context as to how these parameters may affect their results.

After this Introduction, we briefly review our methods for transport calculations in Sec. II. The results, as well as their discussion, are presented in Sec. III. We summarize our work in Sec. IV.

## II. METHODS

### A. The basic equations

The geometry of the system we study is depicted in Fig. 1. The layers are assumed infinite in the transverse, $x$-$z$ plane, and have finite widths in the $y$ direction. This assumption makes the system quasi-one-dimensional. The magnetizations of the outer ($F_1$) and inner ($F_2$) layers are misaligned by an angle $\phi$ in the $x$-$z$ plane. Below, we briefly summarize our methods and procedures which are ultimately based in Ref. [51] and are described extensively in Refs. [14,39].

The Hamiltonian appropriate to our system is

$$\mathcal{H}_{\rm eff} = \int d^3r \Bigg\{ \sum_{\alpha} \hat{\psi}^{\dagger}_{\alpha}(\mathbf{r}) \mathcal{H}_0 \hat{\psi}_{\alpha}(\mathbf{r}) + \frac{1}{2}\Bigg[ \sum_{\alpha,\,\beta} (i\sigma_y)_{\alpha\beta} \Delta(\mathbf{r}) \hat{\psi}^{\dagger}_{\alpha}(\mathbf{r}) \hat{\psi}^{\dagger}_{\beta}(\mathbf{r}) + \text{H.c.} \Bigg] - \sum_{\alpha,\,\beta} \hat{\psi}^{\dagger}_{\alpha}(\mathbf{r}) (\mathbf{h}\cdot\boldsymbol{\sigma})_{\alpha\beta} \hat{\psi}_{\beta}(\mathbf{r}) \Bigg\}, \tag{1}$$

where $\Delta(\mathbf{r})$ is the pair potential, and $\mathbf{h}$ is the Stoner field. The field $\mathbf{h}$ is taken along the $z$ axis in the outer ferromagnetic layer $F_1$ and forms an angle $\phi$ with the $z$ axis in the inner ferromagnetic layer $F_2$. This field is then zero in the superconductor $S$ and normal metal spacer $N$. We have assumed equal magnitude of the fields $h_1 = h_2 \equiv h$ since in the experiments we are considering, the same material is employed for both ferromagnetic layers. $\mathcal{H}_0$ is the single-particle Hamiltonian, and it includes the interfacial scattering. The indices $\alpha$ and $\beta$ denote spin indices and $\sigma_i$ are the Pauli matrices.

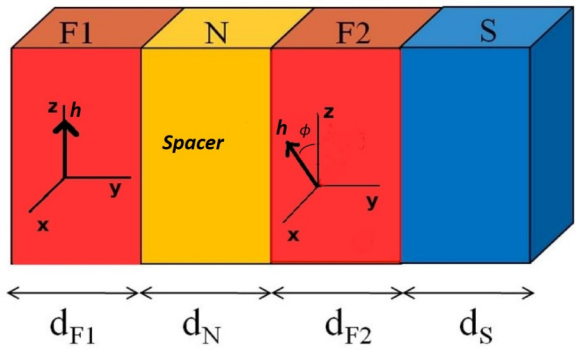


FIG. 1. Scheme of the system studied. The exchange field of the second ferromagnet $F_2$ is rotated in the $x$-$z$ plane by an angle $\phi$. The direction of the transport is in the $y$ direction. The thicknesses are not to scale (see text).

Performing a generalized Bogoliubov transformation, we take $\psi_{\sigma} = \sum_n (u_{n\sigma}\gamma_n + \eta_{\sigma} v^{*}_{n\sigma}\gamma^{\dagger}_n)$ where $\eta_{\sigma} \equiv 1\,(-1)$ for spin down (up), and $u_{n\sigma}(\mathbf{r})$ and $v_{n\sigma}(\mathbf{r})$ are the spin-dependent quasiparticle and quasihole amplitudes. Due to the geometry of the system being quasi-one-dimensional, the spatial dependence on $\mathbf{r}$ becomes a dependence on $y$ alone. Then, we can rewrite the eigenvalue equation corresponding to the Hamiltonian given by Eq. (1) as

$$\begin{pmatrix} H_0 - h_z & -h_x & 0 & \Delta(y) \\ -h_x & H_0 + h_z & \Delta(y) & 0 \\ 0 & \Delta(y) & -(H_0 - h_z) & -h_x \\ \Delta(y) & 0 & -h_x & -(H_0 + h_z) \end{pmatrix} \begin{pmatrix} u_{n\uparrow}(y) \\ u_{n\downarrow}(y) \\ v_{n\uparrow}(y) \\ v_{n\downarrow}(y) \end{pmatrix} = \epsilon_n \begin{pmatrix} u_{n\uparrow}(y) \\ u_{n\downarrow}(y) \\ v_{n\uparrow}(y) \\ v_{n\downarrow}(y) \end{pmatrix}. \tag{2}$$

We use natural units $\hbar = k_B = 1$. The quasi-one-dimensional Hamiltonian is $H_0 = -(1/2m)(d^2/dy^2) + \epsilon_{\perp} - E_F(y) + U(y)$ where $\epsilon_{\perp}$ is the transverse energy, so that Eq. (2) is a set of decoupled equations, one for each $\epsilon_{\perp}$. The energy bandwidth $E_F$ can in principle be layer-dependent. In the $S$ layer, for example, we write $E_F(y) = E_{FS} \equiv k^2_{FS}/2m$. $U(y)$ is the interfacial scattering, which we take to be spin-independent in the form $U(y) = H_1\delta(y - d_{F1}) + H_2\delta(y - d_{F1} - d_N) + H_3\delta(y - d_{F1} - d_N - d_{F2})$ where $H_i$ are the scattering strengths of the respective interfaces. These scattering strengths are best characterized by the dimensionless parameters $H_{Bi} \equiv H_i/v_F$, where $v_F$ is the Fermi speed in $S$. These scattering parameters are quite essential to characterizing possible devices, as even for clean interfaces, some scattering due to residual surface roughness is inevitable. Transport results turn out to be much more sensitive than thermodynamic quantities to interfacial scattering.

All of the calculations must be done self-consistently to preserve charge conservation [14,39]. The self-consistency condition allows for the proper inclusion of the proximity effect, which is of primary importance to our study. It can be written as

$$\Delta(y) = \frac{g(y)}{2} {\sum_n}' [u_{n\uparrow}(y) v^{*}_{n\downarrow}(y) + u_{n\downarrow}(y) v^{*}_{n\uparrow}(y)] \tanh\left(\frac{\epsilon_n}{2T}\right), \tag{3}$$

where $g(y)$ is the superconducting coupling constant in the singlet channel and it is nonzero in the $S$ layer only. The set of eigenvalues is found for each $\epsilon_{\perp}$, and the index $n$ in the sum refers now to all eigenvalues; i.e., it includes summation over $\epsilon_{\perp}$, while the prime symbol indicates that the sum is limited to states with eigenenergies within a cutoff $\omega_D$ from the Fermi level. The self-consistency procedure is this: we

start with a suitable choice for $\Delta(y)$, compute the quasiparticle and quasihole amplitudes using Eq. (2), and obtain $\Delta(y)$ using Eq. (3). Then we repeat this process, substituting the iterated $\Delta(y)$ until the input of Eq. (2) matches the output of Eq. (3). Self-consistency is fundamental in all transport calculations. It is a prerequisite for charge conservation [14,52–54]. From the Heisenberg equation we have

$$\frac{\partial}{\partial t}\langle\rho(\mathbf{r})\rangle = i\langle[\mathcal{H}_{\text{eff}},\rho(\mathbf{r})]\rangle, \tag{4}$$

where $\rho(\mathbf{r})$ is the charge density. In the steady state, and in our geometry, we can rewrite this as

$$\frac{\partial j_y(y)}{\partial y} = 2e\text{Im}\left\{\Delta(y)\sum_n[u^*_{n\uparrow}v_{n\downarrow} + u^*_{n\downarrow}v_{n\uparrow}]\tanh\left(\frac{\epsilon_n}{2T}\right)\right\}. \tag{5}$$

Charge conservation is preserved if $\partial j_y(y)/\partial y$ is identically zero, which is guaranteed when the self-consistency condition Eq. (3) is applied. Another reason why transport is dependent on self-consistency is more obvious: as the pair potential changes, so does the energy spectrum within the superconductor. Proper inclusion of ordinary and Andreev reflection at the interfaces is obviously necessary for a proper account of the transport properties of heterostructures, and the variation of the self-consistent pair amplitudes is most pronounced at the superconducting interface due to proximity effects. Therefore, it is mandatory that we calculate transport using a fully self-consistent pair potential.

### B. Spin transport quantities

The spin-transport-related quantities we consider are the spin current, the STT, and the local magnetization. These are all studied as functions of applied bias voltage $V$. We aim to describe the position dependence of these bias-dependent quantities within the multilayer structure, for a range of relevant values of the geometrical parameters, including $\phi$. In our geometry the spin current is a vector in spin space:

$$S_i \equiv \frac{i\mu_B}{2m}\sum_\sigma\left\langle\psi^\dagger_\sigma\sigma_i\frac{\partial\psi_\sigma}{\partial y} - \frac{\partial\psi^\dagger_\sigma}{\partial y}\sigma_i\psi_\sigma\right\rangle. \tag{6}$$

The spin current density is not a conserved quantity within the ferromagnetic regions. We can relate its gradient to the local magnetization $\mathbf{m} \equiv -\mu_B\sum_\sigma\psi^\dagger_\sigma\sigma\psi_\sigma$, where $\mu_B$ is the Bohr magneton, by writing the continuity equation for the local magnetization in the form

$$\frac{\partial}{\partial t}\langle m_i\rangle + \frac{\partial}{\partial y}S_i = \tau_i,\ i = x,y,z, \tag{7}$$

where $\boldsymbol{\tau}$ is the spin transfer torque $\boldsymbol{\tau} \equiv 2\mathbf{m}\times\mathbf{h}$. In the steady state, $\partial m_i/\partial t$ is zero. This means that the spin current will not be constant within the ferromagnetic layers, and that the local magnetization, even in the steady state, is intrinsically tied to the spin current via the STT.

We can write the magnetization and the spin current in terms of the self-consistent quasiparticle and quasihole amplitudes. In the low-temperature limit, the expression for the local magnetization reads [14]

$$m_x = -\mu_B\left[\sum_n(-v_{n\uparrow}v^*_{n\downarrow} - v_{n\downarrow}v^*_{n\uparrow}) + \sum_{\epsilon_\mathbf{k}<eV}(u^*_{\mathbf{k}\uparrow}u_{\mathbf{k}\downarrow} + v_{\mathbf{k}\uparrow}v^*_{\mathbf{k}\downarrow} + u^*_{\mathbf{k}\downarrow}u_{\mathbf{k}\uparrow} + v_{\mathbf{k}\downarrow}v^*_{\mathbf{k}\uparrow})\right], \tag{8a}$$

$$m_y = -\mu_B\left[i\sum_n(v_{n\uparrow}v^*_{n\downarrow} - v_{n\downarrow}v^*_{n\uparrow}) - i\sum_{\epsilon_\mathbf{k}<eV}(u^*_{\mathbf{k}\uparrow}u_{\mathbf{k}\downarrow} + v_{\mathbf{k}\uparrow}v^*_{\mathbf{k}\downarrow} - u^*_{\mathbf{k}\downarrow}u_{\mathbf{k}\uparrow} - v_{\mathbf{k}\downarrow}v^*_{\mathbf{k}\uparrow})\right], \tag{8b}$$

$$m_z = -\mu_B\left[\sum_n(|v_{n\uparrow}|^2 - |v_{n\downarrow}|^2) + \sum_{\epsilon_\mathbf{k}<eV}(|u_{\mathbf{k}\uparrow}|^2 - |v_{\mathbf{k}\uparrow}|^2 - |u_{\mathbf{k}\downarrow}|^2 + |v_{\mathbf{k}\downarrow}|^2)\right], \tag{8c}$$

where the first terms on the right side are the ground state local magnetization components, and the second terms denote the bias-dependent contributions. We can define a direct analog of the spin accumulation by removing the first terms on the right side $\delta\mathbf{m}(V) \equiv \mathbf{m}(V) - \mathbf{m}(0)$, revealing the change in magnetization due to the finite bias.

We can use the same procedure for the spin current components, Eq. (6), and expand in terms of the $u_n$ and $v_n$ wave functions. In the $T = 0$ limit the result is [14]

$$S_x = \frac{-\mu_B}{m}\text{Im}\left[\sum_n\left(-v_{n\uparrow}\frac{\partial v^*_{n\downarrow}}{\partial y} - v_{n\downarrow}\frac{\partial v^*_{n\uparrow}}{\partial y}\right) + \sum_{\epsilon_\mathbf{k}<eV}\left(u^*_{\mathbf{k}\uparrow}\frac{\partial u_{\mathbf{k}\downarrow}}{\partial y} + v_{\mathbf{k}\uparrow}\frac{\partial v^*_{\mathbf{k}\downarrow}}{\partial y} + u^*_{\mathbf{k}\downarrow}\frac{\partial u_{\mathbf{k}\uparrow}}{\partial y} + v_{\mathbf{k}\downarrow}\frac{\partial v^*_{\mathbf{k}\uparrow}}{\partial y}\right)\right], \tag{9a}$$

$$S_y = \frac{\mu_B}{m}\text{Re}\left[\sum_n\left(-v_{n\uparrow}\frac{\partial v^*_{n\downarrow}}{\partial y} + v_{n\downarrow}\frac{\partial v^*_{n\uparrow}}{\partial y}\right) + \sum_{\epsilon_\mathbf{k}<eV}\left(u^*_{\mathbf{k}\uparrow}\frac{\partial u_{\mathbf{k}\downarrow}}{\partial y} + v_{\mathbf{k}\uparrow}\frac{\partial v^*_{\mathbf{k}\downarrow}}{\partial y} - u^*_{\mathbf{k}\downarrow}\frac{\partial u_{\mathbf{k}\uparrow}}{\partial y} - v_{\mathbf{k}\downarrow}\frac{\partial v^*_{\mathbf{k}\uparrow}}{\partial y}\right)\right], \tag{9b}$$

$$S_z = \frac{-\mu_B}{m}\text{Im}\left[\sum_n\left(v_{n\uparrow}\frac{\partial v^*_{n\uparrow}}{\partial y} - v_{n\downarrow}\frac{\partial v^*_{n\downarrow}}{\partial y}\right) + \sum_{\epsilon_\mathbf{k}<eV}\left(u^*_{\mathbf{k}\uparrow}\frac{\partial u_{\mathbf{k}\uparrow}}{\partial y} - v_{\mathbf{k}\uparrow}\frac{\partial v^*_{\mathbf{k}\uparrow}}{\partial y} - u^*_{\mathbf{k}\downarrow}\frac{\partial u_{\mathbf{k}\downarrow}}{\partial y} + v_{\mathbf{k}\downarrow}\frac{\partial v^*_{\mathbf{k}\downarrow}}{\partial y}\right)\right], \tag{9c}$$

where again the first terms on the right side are the spin current density at zero bias, and the second terms are the contribution from the applied bias. This calculation is independent of that of the local magnetization. Thus we can verify the relation between the STT and the spin current in Eq. (7), as has previously been pointed out [14,39].

### C. Transfer matrix method and spin transport

Here, we give a brief summary of our spin transport calculation methodology. An extensive explanation has been given in Ref. [14]. We review these methods primarily because Ref. [14] focused on charge transport, and it is useful to clarify how they extend to spin transport, which requires some extra care.

The procedure to calculate the conductance $G(V)$ involved merely evaluating the reflection and transmission amplitudes governed by the continuity of the wave function and discontinuity of its derivatives. This has to be done at each interface for both particles and holes, and for each spin, i.e., including both ordinary and Andreev reflection, as one would do in elementary quantum mechanics. In the $S$ electrode, the procedure is [14] to divide it into arbitrarily thin layers, in each of which the $y$-dependent self-consistent pair potential, as previously determined numerically, can be replaced by a constant.

In the expressions for the local magnetization Eq. (8) and the spin current Eq. (9) we have two terms in the right sides. The first is the equilibrium result, and can be calculated straightforwardly by the methods of Sec. II A. The more important terms are, of course, the bias-driven contributions. To evaluate those we have to rebuild the wave functions so that they correspond to the proper boundary conditions of injected spin-up or spin-down particles (see, e.g., Eqs. (4) and (5) of Ref. [14] or Ref. [39]). The method is in essence nothing but the elementary quantum mechanical procedure of building plane wave solutions out of stationary state wave functions, but it is mathematically much more complicated. The procedure is as fully described in Ref. [14] except for the presence of the $N$ layer, which can be included by a trivial extension of either an $F$ layer with $h$ taken to be zero, or an $S$ layer with $\Delta = 0$. The transfer matrix method simply transcribes the continuity conditions for each amplitude, and the discontinuity in the derivatives arising from the delta function interfacial scattering, to each adjacent layer. From these rebuilt wave functions the second terms on the right sides of the expressions for $\mathbf{m}(y)$ and $\mathbf{S}(y)$ are straightforwardly calculated by adding the appropriate contributions. This procedure is especially important in spin transport calculations, as the quantities involved depend on position and the simple BTK [45] procedure that one employs for the conductance does not apply.

## III. RESULTS

### A. General

We report on the spin transport quantities, specifically the spin current, the spin transfer torque, and the bias-dependent portion of the magnetization, which as mentioned above is a measure of the spin accumulation. Each of these quantities depends on the applied bias voltage $V$, which we normalize to $E \equiv eV/\Delta_0$, where $\Delta_0$ is the bulk value of the pair potential in bulk $S$ material. These quantities depend also on the position $y$ within the sample. All lengths are normalized by $k_{FS}$, and normalized lengths are denoted by the corresponding capital letter, e.g., $Y \equiv k_{FS}y$. All energies except for the bias are normalized to the Fermi energy in $S$. The magnetization components $m_i$ are normalized by $-\mu_B(N_\uparrow + N_\downarrow)$, and, correspondingly, the spin current $S_i$ is normalized [14] by $-\mu_B(N_\uparrow + N_\downarrow)E_{FS}/k_{FS}$. The normalization of the scattering strength parameters has been introduced above: values in excess of unity correspond to a tunneling limit situation. We will assume that the two ferromagnetic materials are the same, and hence take the field strengths $h_1$ and $h_2 = h$ to be equal. We will use the value $h = 0.145$ in our dimensionless units. This value was shown to be appropriate to describe the transition temperature [50] of similar samples in which Co was the ferromagnetic material. Similarly, we will assume that the scattering strengths for the two $N/F$ interfaces are the same $H_{B1} = H_{B2} \equiv H_B$. We will take the effective coherence length of the superconducting order parameter to be $\Xi_0 = 115$ which was found to be appropriate for samples in which the $S$ layer was niobium [50]. We set the superconducting layer thickness to be $D_S = 180$, which is large enough compared to $\Xi_0$ to allow for superconductivity, but not so large that the proximity effect is negligible within the superconductor. This has been shown in previous results [39] to provide a more prominent critical-bias feature in charge transport due to the variation in the pair potential $\Delta(y)$. For the same reason, we also take the low-temperature limit $T \to 0$ in our calculations. We will also fix the thickness of the outer ferromagnet to $D_{F1} = 30$ as we have found that the results are less sensitive to this parameter. We will consider variations of $D_N$ and $D_{F2}$. We have assumed that any band mismatch parameters are unity. Although this is not generally true in real systems, in practice the effects of such a mismatch can be incorporated into the effective value of the scattering strength parameter when interpreting and fitting data. This fitting procedure was shown to correctly predict the thermodynamic properties in similar [50] spin valve systems.

Below, we will be showing results for six different sets of the parameters $D_{F2}, D_N, H_B, H_{B3}$. For each set of parameters we will examine the following vector quantities: the spin current, the spin accumulation $\delta\mathbf{m}(V)$, the spatially averaged spin accumulation in $S$ and $N$, and the spatially averaged STT in both $F$ layers. For the first two, we will examine each component at low-bias, $E = 0.6$, and at high-bias values, $E = 2$. We will study the quantities $\delta m_i \equiv m_i(V) - m_i(0)$ and $\tau_i$ as a function of the bias, rather than of position, by averaging these quantities over a layer. Thus, for example $\langle\tau_i\rangle \equiv 1/D_\ell \int dY \tau_i(Y)$ where the integral is over the relevant layer, of thickness $D_\ell$. In all cases we plot the results for several values of the angular mismatch angle $\phi$. The number of quantities involved for each set of physical parameters is excessively large; therefore we focus on only the most remarkable features and angular dependencies, and on their distinctive behavior as a function of the physical parameters.

### B. Ideal interfaces

In Fig. 2 we show the results for a physical parameter set with ideal interfaces (zero interfacial scattering). The layer

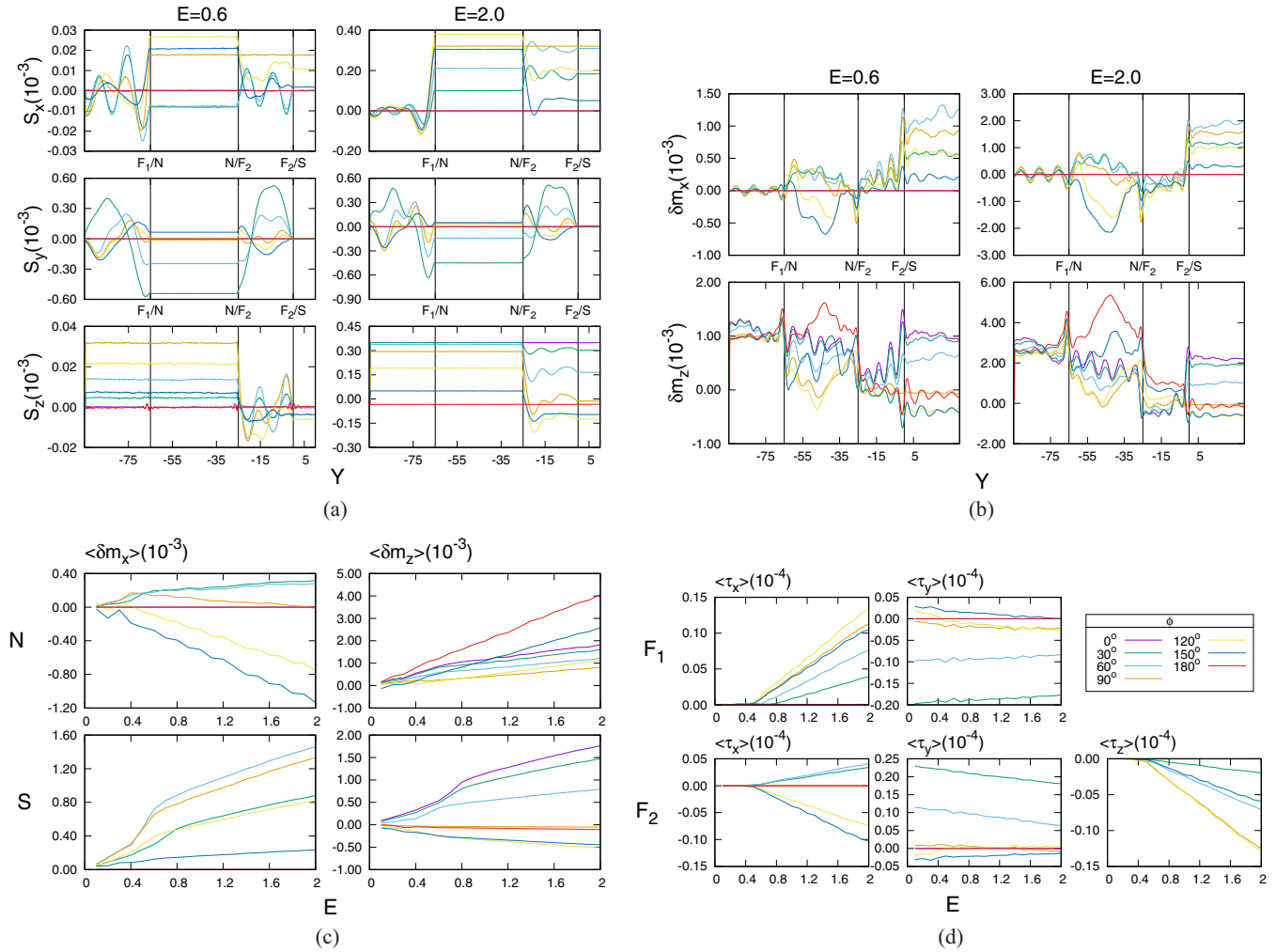


FIG. 2. Results for ideal interfaces. The layer thicknesses for the $F_1/N/F_2/S$ layers are 30/40/25/180, respectively, and the interfacial barriers $H_B$ and $H_{B3}$ are both zero. The key for the angular dependence is in the upper right panel of set (d). See text for details. (a) Local spin current. (b) Local spin accumulation. (c) Spatially averaged local spin accumulation. (d) Spatially averaged spin torque.

thicknesses for the $F_1/N/F_2/S$ layers are 30/40/25/180, respectively. This case can be compared with previous results [39] obtained in some particular cases in the absence of the normal metal layer $N$. The normal layer greatly reduces the STT at the interfaces between the ferromagnets. We start by examining the fundamental features of each quantity mentioned, as a baseline for comparison with subsequent figures. The set of panels labeled (a) show the components of the spin current as a function of position, and the set labeled (b) the spin accumulation, also as a function of position. Sets (c) and (d) refer to the spatially averaged spin accumulation and STT, respectively, as functions of bias.

In Fig. 2(a), we examine the spin current components $S_i$ (top to bottom) as a function of position $Y$ at low to high bias ($E = 0.6$, left and $E = 2$, right). The position of the interfaces is indicated by vertical lines. The origin is taken at the $F_2/S$ interface. Only a small part of the $S$ layer is shown, as the behavior of $\mathbf{S}$ is constant in $S$ beyond the region included. In each panel, we plot the results for seven values of the angle $\phi$, as indicated by the key in the upper right panel of Fig. 2(d). In each case we see that the spin currents at $\phi = 0$ and $\phi = 180^\circ$ are constant, as there are no spin torques when $\mathbf{h_1}$ and $\mathbf{h_2}$ are collinear. Furthermore, $S_x$ for $\phi = 90^\circ$ is constant in $F_2$ since $\mathbf{h_2}$ in this case is along the $x$ axis. Similarly $S_z$ is constant for all $\phi$ in $F_1$ since, with our choice of coordinates, $\mathbf{h_1}$ is along the $z$ axis. As the bias increases, the magnitude of the spin current increases, except for the $y$ component, normal to the layers, which is nearly bias-independent. This is because $S_y$ is driven primarily by the static spin torque that exists near the boundary of the ferromagnetic layers: this torque is entirely in the $y$ direction. We see that $S_y = 0$ for all $\phi$ and all biases within the $S$ layer. This is possibly because the excess current in $S$ is due to triplets, and there are none formed in the $y$ direction. On the other hand, the $S_x$ and $S_z$ components within the superconductor become nonzero at high bias for all angles $\phi$.

These nonzero spin currents in $S$ occur when the applied bias is greater than the critical bias (CB). This bias corresponds to a value smaller than $\Delta_0$: it represents the effective gap energy that the superconductor provides near the interface due to the singlet correlations. The singlet pair amplitudes have previously been shown to be angularly dependent, and the changes in these amplitudes were shown to correspond with the change in critical temperature (see, e.g., Ref. [55], Figs. 2 and 3).

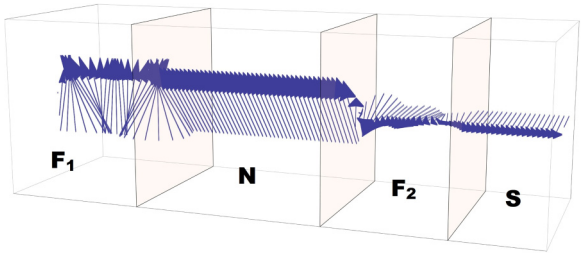


FIG. 3. A 3D representation of the spin current from Fig. 2(a) at $\phi = 90^\circ$ and $E = 2.0$. From left to right, the boxes comprise the layers $F_1/N/F_2/S$, respectively. The spin current precesses about the exchange field in $F$, while also dampening in $F_2$. The orientation of the field in $S$ is rotated to 90° from the $z$ axis.

The reduction or increase in the CB directly correlates to the corresponding change in the singlet amplitudes and thus has a nonmonotonic dependence on $\phi$. This dependence of the CB is due to the proximity effect between the $F_2$ and $S$ layers. The angular dependence comes from the formation of triplet pairs where there is angular mismatch in the system. In this case, with perfect interfaces, the angular dependence of the CB is large, confirming previous results for the charge current [39]. It can be observed that at $E = 0.6$, the critical-bias values for each angle are sometimes above and sometimes below that value of $E$. For angles such that the CB is greater than the bias ($E = 0.6$ in this case), the spin current is zero in the superconductor. However, when the CB is lower than the applied bias, the excitations have energy greater than the effective gap energy and at those angles we find nonzero spin current in $S$.

By viewing the spin current in 3D, we can get a better grasp of its overall orientation within the multilayer. In Fig. 3, in the high bias limit and at $\phi = 90^\circ$, we see that the spin current rotates in the $x$-$z$ plane from near the $z$ direction in $F_1$ to an angle close to the mismatch angle $\phi$ in $F_2$ and $S$. In the ferromagnetic layers, we see the spin current precessing about the exchange fields $\mathbf{h_1}$ and $\mathbf{h_2}$ in $F_1$ and $F_2$, respectively. The precession in $F_2$, however, is damped due to the proximity effect of the superconductor, the current becoming constant at the $F_2/S$ boundary. The spin current in the normal metal layer is also constant, since there are no torques there. The orientation of the spin current in $N$ is rotated in the $x$-$z$ plane to an angle between 0 and $\phi$, with a nonzero $y$-component that is due to the net STT in both ferromagnetic layers.

In Fig. 2(b) we examine the $x$ and $z$ components of $\delta\mathbf{m}$ for low to high biases (left to right) as functions of $Y$. The $y$ component is several orders of magnitude smaller and we do not show it. The component $\delta m_x$ is zero for $\phi = 0$ and $\phi = 180^\circ$. $\delta m_z$ is nonzero and only weakly $\phi$-dependent in $F_1$, whereas $\delta m_x$ is oscillatory and small in this region. Furthermore, $\delta m_z$ and $\delta m_x$ are nonzero and nearly constant with position in the $S$ region at large bias. In general the magnitude of the spin accumulation $\delta\mathbf{m}(V)$ is oscillatory everywhere at low biases, but with small amplitudes. It oscillates in $N$ and irregularly rotates in the $x$-$z$ plane, particularly for mismatch angles near $\phi = 90^\circ$. The overall magnitude increases with bias with very little change in the angular dependence. The spin accumulation vector tends to align with $\mathbf{h_2}$ within the superconductor: this is similar to the spin current behavior. The magnitude of $\delta\mathbf{m}$ also decreases, in all layers, as $\phi$ increases from 0 to 180°.

In Fig. 2(c) we examine the spatial average (as defined earlier in this section) of $\delta\mathbf{m}(V)$ in the $N$ and $S$ layers (upper and lower plots, respectively), as a function of bias. In both regions, $\langle\delta m_x\rangle$ vanishes for $\phi = 0$ and $\phi = 180^\circ$. In $S$ we can see a critical-bias behavior in $\langle\delta m_x\rangle$, at which value the magnitude begins to rise quickly with bias, becoming approximately linear. In both regions each component is nonmonotonic in $\phi$. In $S$ $\langle\delta m_x\rangle$ is maximized between $\phi = 60^\circ$ and $\phi = 90^\circ$ while in $N$ it is most negative at $\phi = 150^\circ$; $\langle\delta m_z\rangle$ features a similar but less dramatic critical-bias feature only in $S$, with this component decreasing for angles $\phi > 90^\circ$.

In Fig. 2(d) we consider the average spin transfer torques as a function of $E$, as just done with the average spin accumulation. We do so only in the ferromagnetic regions where the torques are nonzero. The component $\tau_z$ is zero in the outer ferromagnetic region $F_1$, since the field $\mathbf{h_1}$ is along the $z$ direction, and it is not plotted: the angular key for the entire figure is shown instead. The torque $\tau$ is always zero for $\phi = 0$ and $\phi = 180^\circ$, and $\tau_x = 0$ for $\phi = 90^\circ$ in $F_2$: this follows from our geometry. We see a strong critical-bias feature in the $x$ component in both $F_1$ and $F_2$, and also in the $z$ components in $F_2$: the averaged torque is zero below the CB, and then grows linearly with increasing bias. The $x$ component in $F_1$, and the $z$ component in $F_2$, show similar behavior, with a steady increase or decrease in value, respectively, for all angles, and a maximum magnitude between $\phi = 90^\circ$ and $\phi = 120^\circ$. $\langle\tau_x\rangle$ in $F_2$ is different: it increases with $E$ for angles $\phi < 90^\circ$ and decreases for angles $\phi > 90^\circ$. $\langle\tau_y\rangle$ has very different behavior from both of the other components: it is nonzero at zero bias due to the static ferromagnetic proximity effect. Because of this, $\langle\tau_y\rangle$ is nearly independent of bias, slightly decreasing in magnitude in both ferromagnetic regions. It follows from Eq. (7) in the steady state that the net change in spin current in $N$ and $S$ is directly proportional to the average torque. Indeed, the constant $S_y$ in the normal metal can be described by the net average torque $\tau_y$ in both ferromagnetic regions.

In this subsection we have analyzed the the spin current and spin accumulation for the ideal interface case. Although such perfect samples cannot be fabricated, much that is learned in this simple case can be applied to more realistic systems. A good part of the discussion for Fig. 2 will apply to the results for other physical parameter values presented below. We have seen that in the high-bias limit the spin current precesses in the $F$ layers about the respective internal exchange fields $\mathbf{h_i}$, while being a constant in $N$ and $S$ with an orientation determined by that of the neighboring exchange fields of the ferromagnets. We also see that the in-plane components of the spin current ($S_x$ and $S_z$ in our coordinate system) are bias-dependent, and the plane-perpendicular component ($S_y$) is bias-independent. The latter is due to the proximity effect between the two ferromagnetic layers, which produces a torque solely in the $y$ direction without an applied bias. More remarkable is the bias dependence in the $x$ and $z$ components of the spatially averaged spin torque, which shows a critical-bias behavior of its own. Above the CB value, the magnitude of the torque and the spin current increases linearly, while below there is no bias dependence. This is similar to the charge current behavior in the tunneling limit. Consistent with this, there is no penetration of

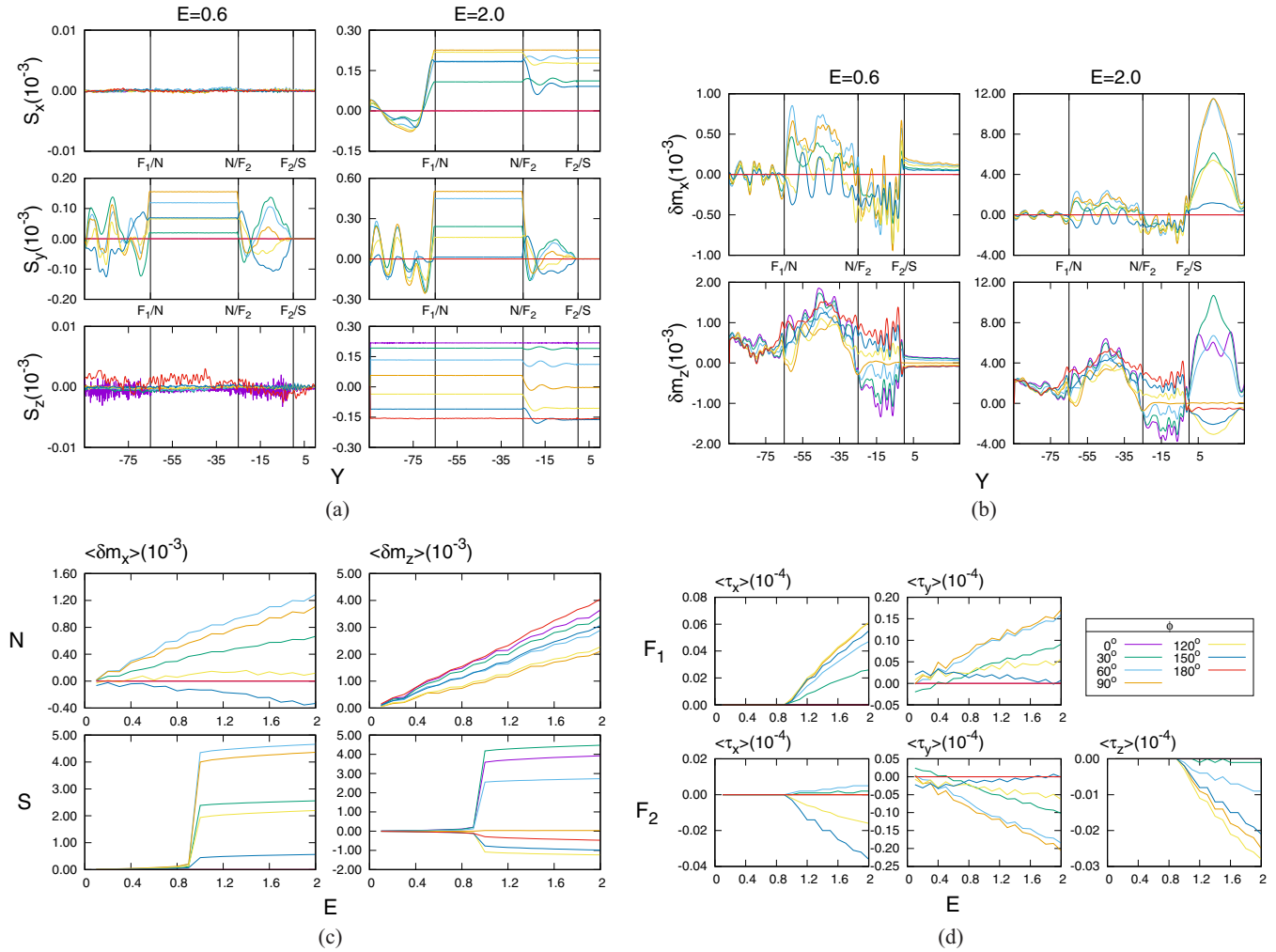


FIG. 4. Results for a nonzero tunneling barrier at the $F_2/S$ interface. The layer thicknesses are as in Fig. 2 and the interfacial barriers are $H_B = 0$ and $H_{B3} = 0.9$. See text for details. (a) Local spin current. (b) Local spin accumulation. (c) Spatially averaged local spin accumulation. (d) Spatially averaged spin torque.

the spin current within the superconductor below this CB. The spin accumulation behaves similarly to the spin current, but is not constant in magnitude in $N$ or $S$, nor in orientation within $N$, and the overall behavior is highly oscillatory. The spatially averaged local $\delta\mathbf{m}(V)$ also features a CB feature, separately from that of the torque. For this ideal case, the bias feature is less pronounced than in the nonideal case (see below), but a clear transition can be seen in the quasilinear bias trends below and above the bias thresholds that are not obviously related to those of the spin current features.

### C. Interfacial scattering

We now turn on the effect of interfacial scattering. First we consider, in Fig. 4, the case where only a barrier at the $F_2/S$ interface exists, with a qualitatively large scattering parameter value $H_{B3} = 0.9$. The layer thicknesses are as in the previous figure. When the scattering is large at this interface, the superconducting proximity effect is reduced. We compare this case to the zero-scattering limit of Fig. 2 in order to examine closely how the basic features of the proximity effect influence the spin currents. The organization of the panels in Fig. 4 is the same as in Fig. 2.

In Fig. 3(a) we see that the $x$ and $z$ components of the spin current are now driven to zero, within numerical precision, at low bias. This is due to the increase in the CB due to the barrier, which weakens the proximity effect and thereby makes it more difficult for the Cooper pairs to propagate out of the superconductor and convert to long-ranged triplets. The $y$ component, however, is still nonzero due to the static spin torques from the ferromagnetic proximity effect. Unlike in the other cases discussed, $S_y$ now increases significantly at higher biases, although not as dramatically as the other two components. In the high-bias regime, the system returns to precessing about $\mathbf{h}$ in the ferromagnetic regions. $\mathbf{S}$ is also rotated about the $x$-$z$ plane, this time closer to the second ferromagnetic field $\mathbf{h_2}$ which is oriented at an angle $\phi$. The overall magnitude of the spin current is of course reduced by the barrier.

In Fig. 3(b) we see that the spin accumulation is significantly decreased in magnitude within the superconductor at the low-bias limit. The magnitude increases dramatically in $S$ at high bias, although it remains smaller than for perfect interfaces.

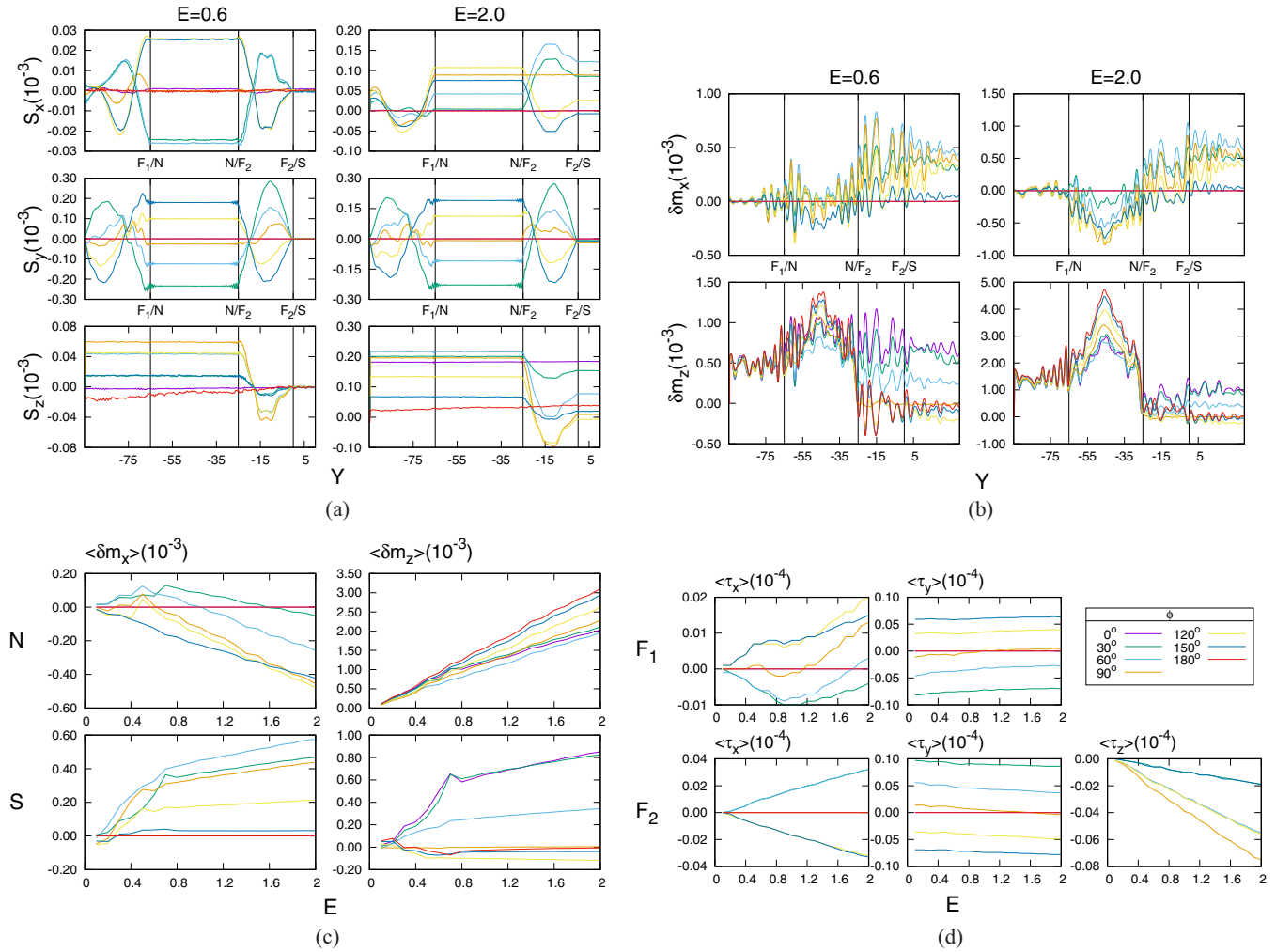


FIG. 5. Results for nonzero barriers in the $F_1/N$ and $N/F_2$ interfaces. The layer thicknesses are as in Figs. 2 and 4. The interfacial barriers are $H_B = 0.5$ and $H_{B3} = 0$. See text for details. (a) Local spin current. (b) Local spin accumulation. (c) Spatially averaged local spin accumulation. (d) Spatially averaged spin torque.

Furthermore, we see that the magnitude of $\delta\mathbf{m}$ is highly oscillatory in the superconductor. The orientation remains fixed to that of the exchange field $\mathbf{h_2}$. In the normal metal, the spin accumulation rotates counterclockwise within the $x$-$z$ plane for $\phi < 90^\circ$ and then reverses direction to become aligned with the $z$ axis again for $\phi = 180^\circ$. The rotation in the $x$-$z$ plane is uniform throughout the $N$ layer in the high-bias case, but not for low-bias values. In the spatially averaged results of Fig. 3(c) we note a remarkable feature in the superconducting layer: a dramatic, sharp increase in the magnitude of $\langle\delta\mathbf{m}\rangle$ at the critical bias, after which the magnitude grows at a much slower rate. The angular dependence remains approximately the same as in Fig. 2(c). The low-bias spin accumulation is heavily impeded by the high barrier. In Fig. 3 we show that the average STT exhibits the same critical-bias features as in Fig. 2(d). However, the high barrier causes the critical bias to increase and to become nearly $\phi$-independent. Its value is seen to be $E \approx 0.85$ in the results for $\langle\tau_x\rangle$ (in both $F_1$ and $F_2$) and for $\langle\tau_z\rangle$ in $F_2$. Furthermore, $\langle\tau_x\rangle$ in $F_2$ shifts to become almost entirely negative. The $y$ component is changed dramatically by the barrier: $\langle\tau_y\rangle$ steadily increases in magnitude with increased bias for all angles except $\phi = 150^\circ$. The static spin torque is heavily reduced by the introduction of a large barrier between $F$ and $S$, which increases the pair potential at the interface.

In Fig. 5 we turn to the converse case where the scattering potentials at both of the $F/N$ interfaces are nonzero, while the $F_2/S$ barrier is ideal, thereby complementing the study in the previous figure. The layer thicknesses are again 30/40/25/180. For the interfacial barriers we take $H_B = 0.5$ (a value not so high as to be in the tunneling limit) and $H_{B3} = 0$. Thus, there is a full proximity effect between $S$ and $F_2$. We now are interested in how the scattering within the spin valve structure affects the spin transport. Perhaps unsurprisingly, the introduction of these barriers turns out to be very important, as the spin valve effect, which determines much of the spin transport features, is quite sensitive to these scattering potentials. In Fig. 5(a) we see that the spin current is nonzero in the $N$ region at low bias, as in the zero-barrier case. $S_y$ in $N$ is now almost entirely bias-independent and its angular dependence is symmetric about $\phi = 90^\circ$, positive for $\phi > 90^\circ$ and negative for $\phi < 90^\circ$. Similarly, the $\phi$ dependence of $S_x$ at low bias is nearly symmetrical with respect to $\phi$ in all layers. At high bias, we again see that the $x$ and $z$ components of the spin current increase, penetrating the superconductor. Due

to the significant interfacial scattering, the overall magnitude decreases from the zero-barrier case, especially for the $x$ and $z$ components.

In Fig. 5(b) we see that, in comparison to the corresponding perfect interface case of Fig. 2(b), the angular dependence is decreased in the normal metal layer, with more oscillations in $\delta m_x$ about the zero value and a peak forming in $\delta m_z$ in both the low and high bias cases. In Fig. 5(c) we see that the average spin accumulation in $S$ has an angular dependence and critical-bias features similar to those found in the zero-barrier case, but with decreased magnitude. An exception is for the $x$ component at $\phi = 150^\circ$, which is significantly larger. In the normal metal, $\langle \delta m_x \rangle$ increases up to a $\phi$-dependent CB, then steadily decreases for increasing bias. $\langle \delta m_z \rangle$ monotonically increases with bias, and has a greater magnitude than $\langle \delta m_x \rangle$. In Fig. 5(d) we see significant differences in the behavior of the average STT, as compared to the single high-barrier case of Fig. 4(d). $\langle \tau_x \rangle$ in $F_1$ no longer features a CB behavior: it is nearly constant with $E$. In both ferromagnets, $\langle \tau_y \rangle$ is again only weakly dependent on bias, with a slight increase in the $F_1$ layer and a decrease in the $F_2$ layer. The overall magnitude is significantly smaller, in all layers and for all components, than in the zero-barrier case. In $F_2$, we see a remarkable symmetry emerge in the angular dependence of the averaged $\tau_x$ and $\tau_z$. For $\langle \tau_x \rangle$, the values for $\phi = 30^\circ$ and $\phi = 60^\circ$ are both increasing and positive, while those for $\phi = 120^\circ$ and $\phi = 150^\circ$ are decreasing by an equivalent amount. Similarly, for $\langle \tau_z \rangle$, we see an equivalent decrease in value with increasing bias for supplementary angles ($\phi = 30^\circ, 150^\circ$ and $\phi = 60^\circ, 120^\circ$).

In Fig. 6 we finally examine the relevant situation where there are scattering barriers at all interfaces. Thus, in addition to the two interfacial scattering barriers with $H_B = 0.5$ in Fig. 5 we include an additional scattering barrier at the $F_2/S$ interface, with $H_{B3} = 0.3$. Although it is reasonable to assume that efforts will be made to minimize the scattering at this interface, unavoidable experimental limitations and wave vector mismatch (as mentioned above) imply that one can never assume that any barrier will perfectly vanish. The layer thicknesses are as in the previous figures. The organization of this figure is simplified, when compared to the previous ones. The local spin current is not shown in Fig. 6 because it is very similar to that in Fig. 5(a). We see then that the introduction of a third barrier of intermediate size at the $F_2/S$ interface does not significantly affect the spin current. The spin transfer torques also remain unaffected: this is because the proximity effect is not seriously inhibited by this additional barrier, and the spin valve effect dominates the spin transport, in these cases. Hence, the sets of panels corresponding to (a) and (d) in the previous figures are omitted, and we focus in this figure on the spin accumulation and its spatial average, panels (b) and (c) in the previous figures, now in the top four and bottom four panels, respectively. The color key for the $\phi$ dependence is as indicated in Figs. 2(d) and 4(d).

In the top panels we see that $\delta\mathbf{m}$ in the normal metal layer departs significantly from what we found in Fig. 5(b) at $H_{B3} = 0$. In $\delta m_z$ we observe a transition from the single-peak result seen in Fig. 5(b) to a triple-peak structure particularly prominent for $\phi < 90^\circ$. The $x$ component also forms three peaks at low and high biases in $N$, at all angles. As in the previous cases, $\delta\mathbf{m}$ is rotated in the $x$-$z$ plane in $N$. However,

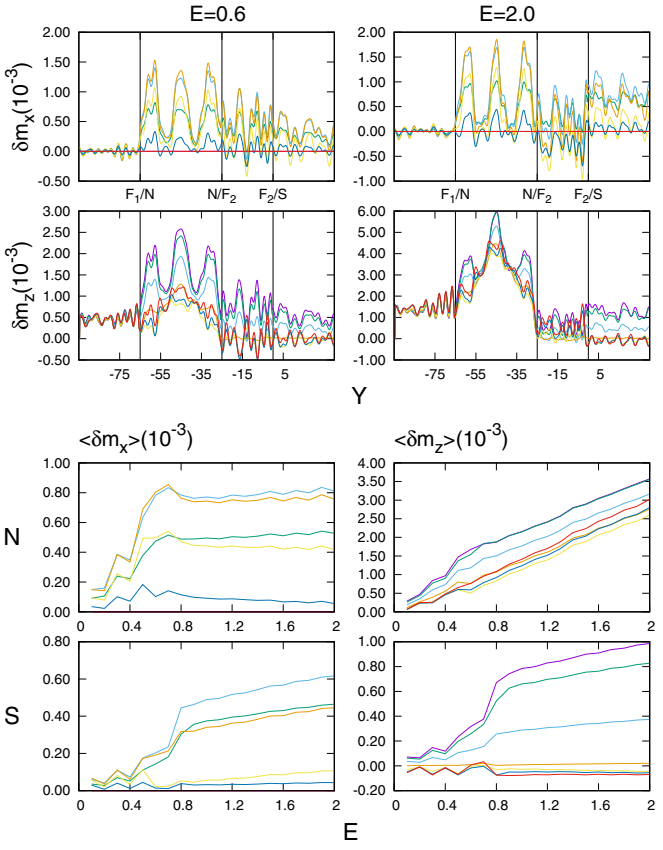


FIG. 6. Results with nonzero interfacial barriers at all interfaces. The layer thicknesses are as in the previous figures, and the interfacial barriers are $H_B = 0.5$ and $H_{B3} = 0.3$. The top four panels are the local spin accumulation, and the bottom four panels are the spatially averaged spin accumulation. The color key for the angular dependence is as in Fig. 2(d). See text for details.

these rotations are nonuniform, and strongly nonsinusoidal, with the troughs aligning with the $z$ axis while the peaks align at an angle less than the mismatch angle $\phi$.

In the bottom panels we see in $\langle \tau_i \rangle$ an enhancement in the critical-bias feature in $S$ seen in Fig. 5(c), reflecting that the low-bias conductance is depressed in this case [39]. There is a steep growth in the magnitude of $\delta\mathbf{m}$, averaged in $S$, at the critical bias. In the normal metal, we see a behavior for $\langle \delta m_z \rangle$ similar to that in Fig. 5(c) but with a remarkably different angular dependence. For $\langle \delta m_x \rangle$ in $N$ we see a very different high-bias behavior, where $\langle \delta m_x \rangle$ increases dramatically at the critical bias and then abruptly levels off to a flat or slightly decreasing bias dependence. The behavior in the average $\delta m_x$ in $N$ is now much more similar to that of $\delta m_x$ or $\delta m_z$ in $S$.

The dependence of the spin current and $\delta\mathbf{m}(V)$ on interface quality, which we have considered in this subsection, is particularly important, not only because ideal interfaces are not possible, but also because interfacial quality cannot be perfectly replicated between samples. Therefore, understanding this dependence is vital to explain differences in measured quantities of similarly constructed samples. We started with a tunneling barrier between the $F$ and $S$ layers, which produced results that differ greatly from the more ballistic, low-barrier cases, both for the spin current and the spin accumulation.

We find a stronger critical-bias behavior in the spin current and torque, where the CB moves to unity in our units. This is because of the weakening of the proximity effects in the tunneling limit. The spin current is strongly driven to zero for bias values below the CB. The spin accumulation in the $S$ region is similarly driven low below this value, but no such strong CB feature is seen in the local $\delta\mathbf{m}(V)$ within the normal metal. The behavior in the tunneling limit directly contrasts with that found for the intermediate barrier strengths of the next two cases (barriers $H_B = 0.5$, $H_{B3} = 0$ and $H_B = 0.5$, $H_{B3} = 0.3$ respectively) whose spin current features are similar to each other. We see a vanishing CB effect in the magnitude of the spin current and torque in $F$, possibly due to resonance effects in the intermediate barriers. However, we do still see a CB effect in the penetration of the spin current into the superconductor, as found for the ideal barrier case. In both cases, we also see a prominent, although weaker, critical-bias effect in the local $\delta\mathbf{m}(V)$ in the $S$ layer. However, we also see a CB effect in the normal metal, absent in the tunneling case. The behavior of the local spin accumulation in $N$ depends on the value of $H_{B3}$. There is a regular oscillatory pattern in $\delta\mathbf{m}(V)$ for nonzero $H_{B3}$ that results in three peaks that have a regular rotation in orientation within the normal metal. This leads us to conclude that the critical-bias behavior of the spin accumulation in $N$ is distinguishable from that of the spin current. We also see a completely new phenomenon in the oscillatory local spin accumulation that is bias-independent but dependent on the physical parameters of the system.

### D. Dependence on layer thickness

In the next two figures, Fig. 7 and Fig. 8, we consider the dependence of the results on geometry, i.e., on layer thickness. We examine a situation where the top four panels are the local spin accumulation, and the bottom four panels are the spatially averaged spin accumulation. The scattering barriers are all nonzero and have the same values as in Fig. 6, namely $H_B = 0.5$ and $H_{B3} = 0.3$, but we now vary the intermediate layer thicknesses of the normal metal, $D_N$ (Fig. 7), and then that of the the inner ferromagnet, $D_{F2}$ (Fig. 8). The layer thicknesses of the $F_1$ and $S$ layers remain $D_{F1} = 30$ and $D_S = 180$ in both figures. In Fig. 7 we increase the normal metal layer spacing from the previous value $D_N = 40$ to $D_N = 60$, leaving $D_{F2} = 25$, while in Fig. 8 we decrease the inner ferromagnetic layer thickness from $D_{F2} = 25$ to $D_{F2} = 15$, while leaving $D_N = 40$. Geometric changes can strongly affect the transmission and reflection amplitudes, just as they do in elementary quantum mechanics problems such as that of transmission across two barriers, where the results can depend drastically on the separation between the two scattering centers. Here we examine how these rather minor changes in the geometry affect the spin transport quantities. We have found little change in the spin current and spin torque when increasing $D_N$; thus in Fig. 7 we only include plots of the spin accumulation and its average, following the scheme of Fig. 6, in the top four and bottom four panels, respectively. For Fig. 8, on the other hand, we include the results for spin current and torque components as we find nontrivial changes in the magnitude and orientation of the spin current, following then the organizational scheme of Figs. 2, 4, and 5.

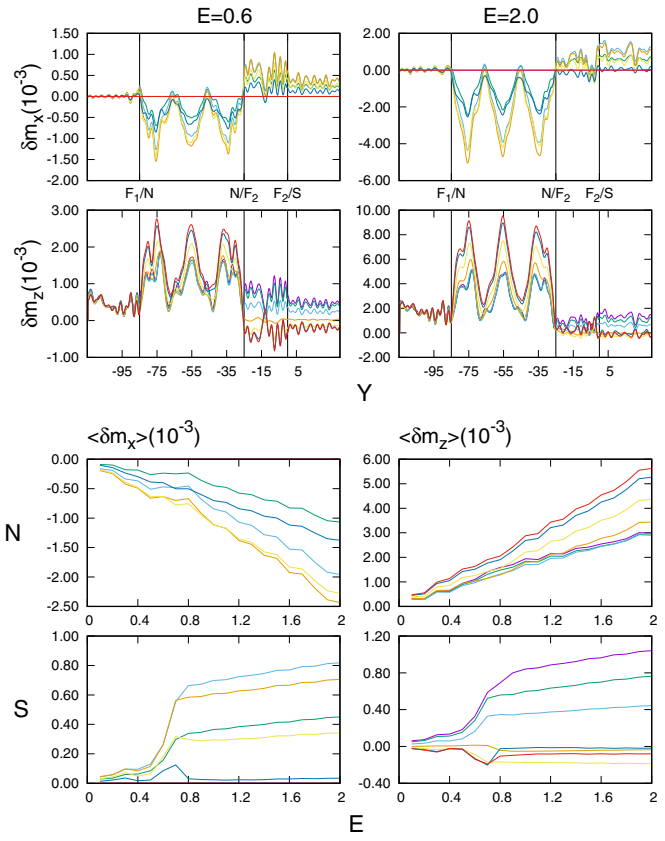


FIG. 7. Results with an increased normal metal layer thickness, emphasizing the $D_N$ dependence. The layer thicknesses for the $F_1/N/F_2/S$ layers are 30/60/25/180, respectively, and the interfacial barriers $H_B$ and $H_{B3}$ are 0.5 and 0.3, respectively. The top four panels are the local spin accumulation, and the bottom four panels are the spatially averaged spin accumulation. The color key for the $\phi$ dependence is as in, e.g., Fig. 2(d).

In the top panels of Fig. 7 we observe a three-peak structure for the spin accumulation in $N$ similar to that found in the top panels of Fig. 6, but with several distinctions. First, we see that $\delta m_z$ has now fully transitioned to the three-peak behavior for all $\phi$ and all biases. Also, the three-peak behavior is inverted in $\delta m_x$. Indeed, $\delta\mathbf{m}$ makes now a clockwise rotation in the $x$-$z$ plane in $N$, contrary to both the spin current and spin accumulation behaviors we have seen thus far. The orientation in $S$ remains unaffected. We also see a significant increase in the magnitude of $\delta\mathbf{m}$ in all layers for high biases, indicating greater growth in the spin accumulation. In the bottom panels we see a behavior in the average spin accumulation in $S$ similar to that in the bottom panels of Fig. 6, with increases to the $x$ component for angles $\phi = 30^\circ$, $90^\circ$, and $120^\circ$. The behavior in $N$ is significantly different from that found in the previous cases, where in the $x$ component we now see no major critical-bias behavior and a steadily decreasing bias dependence: this is now similar to the behavior of the magnitude of the $z$ component. The $z$ component has the usual steady increase with bias, but the angular dependence is now most similar to that in Fig. 5(c). We see then that the angular dependence is very sensitive to both the layer thickness and the barriers.

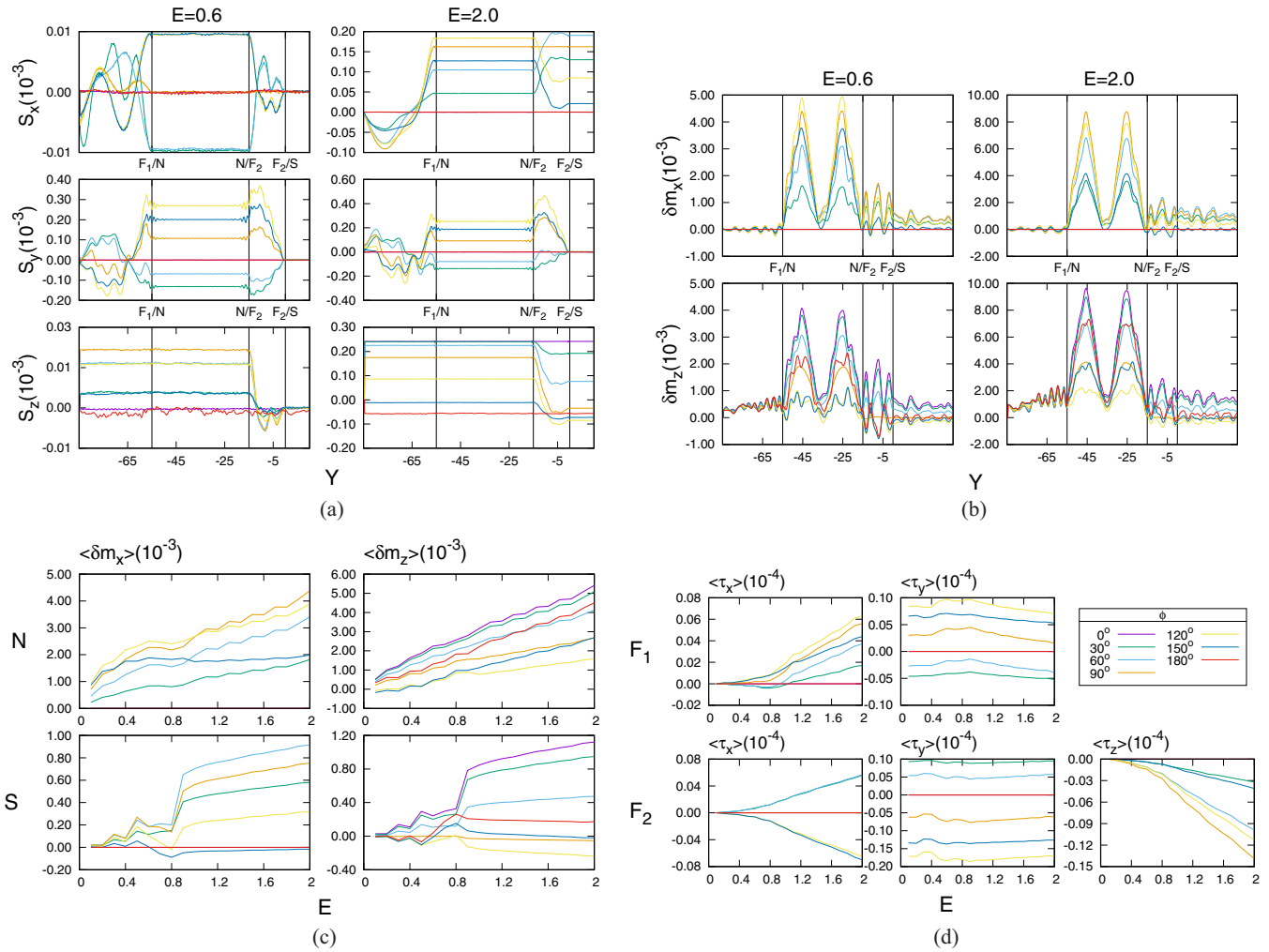


FIG. 8. Results with a decreased intermediate ferromagnetic layer thickness, emphasizing the $D_{F2}$ dependence. The layer thicknesses for the $F_1/N/F_2/S$ layers are 30/40/15/180, respectively, and the interfacial barriers are $H_B = 0.5$ and $H_{B3} = 0.3$. (a) Local spin current. (b) Local spin accumulation. (c) Spatially averaged local spin accumulation. (d) Spatially averaged spin torque.

For Fig. 8 we revert to the full set of plots used, e.g., in Fig. 2, with the same internal organization. In Fig. 8(a) we see [when comparing with the results shown in Fig. 5(a) which, as mentioned, are quite similar to those for the case shown in Fig. 6] that when decreasing the intermediate ferromagnetic layer spacing, the $x$ and $z$ components of the spin current decrease quite significantly in the low-bias limit, but on the other hand, they increase somewhat in the high-bias limit, especially the $S_x$ component. The orientation of $\mathbf{S}$ in the superconductor is now rotated closer to the negative $z$ direction, much more significantly so for orientations with $\phi > 90^\circ$. This feature is complemented by Fig. 8(d), where the average spin torque is seen to increase its rate of growth. This may seem counterintuitive at first, but it is important to note that the superconducting pair amplitudes are damped by the ferromagnetic layer.

In Fig. 8(b) we see, comparing now directly with Fig. 6, that decreasing $D_{F2}$ changes the spin accumulation in $N$ from a three-peak to a two-peak structure with the same angular dependence and greater magnitude. The peaks also show a greater rotation in orientation compared to those in Fig. 6, where the spin accumulation is more closely aligned to the orientation of $\mathbf{h_2}$ than before. The troughs of these oscillations are still oriented along the $z$ axis. The overall magnitude of the spin accumulation also increases dramatically with bias, at a much greater rate than those in the systems discussed previously, as can be seen in Fig. 8(c). However, $\langle \delta m_x \rangle$ in $N$ steadily increases with bias, with a slight peak near the critical bias. The average spin accumulation at angle $\phi = 150^\circ$ does not increase with bias, and remains an outlier.

In considering the geometry dependence in this subsection, we have focused on the thickness of the intermediate layers, as these tend to be the thinnest in actual systems and the impact of small deviations in the design and fabrication process needs to be understood. We have found previously that these layers have the greatest impact on charge transport [39]. However, we see almost no dependence of the spin current on the normal metal layer thickness (see Fig. 6 and Fig. 7). This is likely due simply to this layer being nonmagnetic. The spin accumulation shows a similar critical-bias behavior and a three-peak oscillating pattern in the normal metal layer, but with a curious distinction: the orientation, and in general the $x$ component bias dependence, of $\delta\mathbf{m}(V)$ reverses direction, rotating $\delta\mathbf{m}$ clockwise in the $x$-$z$ plane in $N$. This is in the

opposite direction of the general rotation between the $\mathbf{h_1}$ and $\mathbf{h_2}$ exchange fields. We have not yet determined why this may happen and it warrants further study. We do find a strong dependence on the spin current on the intermediate ferromagnetic layer thickness $D_{F2}$. By decreasing $D_{F2}$, we see a reemergence of the CB effect in the spatially averaged torque, as well as greater growth of the spin current magnitude with bias. We also see a dramatic change in the spin accumulation in $N$, where, comparing Fig. 6 to Fig. 8, changes in the oscillation of the local spin accumulation occur, resulting in only two peaks. These figures are for the same $D_N$ and the same value of the exchange field. We conclude that the $D_{F2}$ dependence is the most important layer thickness quantity for the spin current and spin transport torque properties of the system, whereas the spin accumulation is highly dependent on both the $D_N$ and $D_{F_2}$, in addition to the interfacial scattering dependence as was seen in the previous subsection.

## IV. CONCLUSIONS

We have investigated spin transport for $F/N/F/S$ superconducting spin valves. Through our study, we have predicted the main characteristics of the relevant spintronic quantities, namely the spin current, the spin transfer torque, and the local magnetization (a proxy for spin accumulation). We have done so for multiple variations of the geometrical and interfacial parameters of the spin valve. Our focus has been on clean samples with thicknesses similar to those that have been fabricated, and which include a normal metal spacer and reasonably good interfaces. The material parameters employed, such as internal field and coherence length, have been shown to be valid for such samples where Nb is the superconductor, Cu the normal spacer, and Co the ferromagnet: these values were successfully used previously to quantitatively fit, using our theoretical methods, the transition temperatures [50] of similar spin valve heterostructures. This quantitative success makes us confident as to the validity of the predictions presented here. Our main results are given as a function of position within the spin valve, and of the applied bias. We consider both low-bias values and the high-bias limit where the bias exceeds the bulk superconductor gap. We emphasize the dependence of all results on the misalignment magnetization angle $\phi$ between the $F$ layers; the misalignment determines the triplet pair formation, hence the range of the proximity effects and indeed the valve action. Our analysis includes variation of the interfacial scattering parameters and intermediate layer thicknesses to better encompass a full picture of possible real-world results. However, the parameter space is exceedingly large with no possible extrapolation due to the oscillatory behavior of many quantities and the complexity of the self-consistent calculations required. Therefore, what we present here is merely a subset of our results with the expressed purpose of establishing the main characteristics of the outcomes and exhibiting a glimpse of the richness and variety of what can be done.

Our results are presented in detail in Sec. III. We begin by discussing the the dependence of the results on the scattering potential barriers that would be prevalent in even the most ideal fabrication processes. Then, starting with a realistic geometry, we vary the intermediate layer thicknesses while keeping them within an experimentally realistic range. In our results we see a distinct critical-bias behavior where, for a certain value of the bias, which is in general $\phi$-dependent and always smaller than the bulk $S$ gap value, the spin transport behavior changes, with both the spin current and the spin accumulation beginning to penetrate into the superconductor. By analyzing the spatially averaged spin accumulation and STT within each layer, we also see the critical-bias behavior featured in the magnitude of these quantities. We are then able to analyze the trends both above and below the critical bias. These averages show distinct growth in the spin accumulation in $S$, and also in $N$ for certain sets of both interfacial scattering and thickness parameters. The spin transfer torque also shares this behavior within the ferromagnetic regions, with an additional symmetrical behavior in the angular dependence when the interfacial barriers are fully introduced.

We also observe, at fixed higher bias, the spatial precession of the spin current within the ferromagnets due to the spin transfer torque. The spin current precesses about the internal field of the ferromagnet, with a decaying amplitude within the intermediate $F_2$ layer due to the proximity effect of the superconductor. This results in both the spin current and the spin accumulation being oriented within the superconductor at an angle near the field misalignment angle $\phi$, and at an angle between zero and $\phi$ within the normal metal layer. This is only one way in which the misalignment angle plays a factor. Indeed, the critical-bias features are angularly dependent chiefly because of the angular dependence of the triplet amplitudes, resulting in a very complex and in general nonmonotonic behavior in $\phi$ for all of our spin transport quantities. The angular dependence of the critical bias was already exhibited in our previous results [39] for the charge current, and they correlate with the critical-bias features found in the averages.

Another noteworthy feature of the spin accumulation occurs within the normal metal layer, where the system transitions, as parameters vary, from a situation where the magnitude of this quantity has a single peak at the center of the normal layer, to multiple-peak behavior. We find that by varying *either* the interfacial scattering parameters *or* the normal metal layer thickness, we get a transition into a three-peak behavior. Naively, one would assume this to be due to the to the normal quantum mechanical effects of the spacial oscillations alone. However, by varying the thickness of the intermediate ferromagnetic layer $D_{F2}$, we see a two-peak behavior for the same normal metal layer thickness and interfacial scattering values. This is unique to these spin valve systems, which are highly sensitive to the exact set of parameters, both geometrical and physical. Indeed, the spatial spin current and spin accumulation features cannot be extrapolated to trends within the set of parameters we have analyzed. However, the average quantities of the spin accumulation and spin transfer torque may be at least sometimes extrapolated at high-bias values, as the spatial averages tend to be quasilinear in this limit.

Thus, we have calculated both the spin current and spin accumulation in superconducting spin valves for a set of experimentally relevant parameters. The dependencies of these quantities on the parameters (including the misalignment angle $\phi$) are complex, nonmonotonic, and extremely rich in features. Many of these features are not yet fully understood, and only the most prominent ones have been discussed in this work to

a sufficient extent. In the greater context, we can make a few general conclusions: The spin current and spin transfer torque are the more stable quantities under small variations of the physical parameters, when compared to the spin accumulation. This suggests that reproducible experimental measurements of the spin current can be more easily realized than those of the spin accumulation. We see no penetration of the spin current below the critical bias. We find a critical-bias feature in the quasilinear growth of the spin current and spin torque both above and below the CB. The value of the CB varies with $\phi$, as it does for charge current, which reflects that it is determined largely by the equilibrium behavior of the pair potential. The prominence of the features observed varies with interfacial scattering and with the intermediate ferromagnetic $F_2$ layer thickness. The spin accumulation is highly dependent on the physical parameters. The CB features of the local magnetization are different from those of the spin and charge current, and have a greater dependence on the interfacial barrier strengths. We also see a peculiar behavior in the normal metal region: regular oscillations and rotations of the spin accumulation vector emerge when the interfacial scattering is nonzero. The wavelength of these oscillations and their orientation depend on the thickness of the $F_2$ and $N$ layers. This phenomenon merits further study both theoretically and experimentally.

We expect these results to be a footstool on which more understanding can be developed of the spin transport properties of these nanoscale superconducting spin valves, both through experiment and through continued theoretical work.

## ACKNOWLEDGMENTS

The authors thank Ilya Krivorotov (Irvine) and Chien-Te Wu (National Chiao Tung University) for many helpful discussions. This work was supported in part by US Department of Energy Grant No. DE-SC0014467.

[1] E. Tsymbal and I. Žutić, *Handbook on Spin Transport and Magnetism* (CRC Press, Boca Raton, FL, 2012).
[2] M. Johnson, Phys. Rev. Lett. **70**, 2142 (1993).
[3] F. J. Jedema, A. T. Filip, and B. J. van Wees, Nature (London) **410**, 345 (2001).
[4] J. C. Slonczewski, J. Magn. Magn. Mater. **159**, L1 (1996).
[5] L. Berger, Phys. Rev. B **54**, 9353 (1996).
[6] E. B. Myers, D. C. Ralph, J. A. Katine, R. N. Louie, and R. A. Buhrman, Science **285**, 867 (1999).
[7] S. Bhatti, R. Sbiaa, A. Hirohata, H. Ohno, S. Fukami, and S. N. Piramanayagam, Mater. Today **20**, 530 (2017).
[8] M. Eschrig, Phys. Today **64**(1), 43 (2011).
[9] M. Eschrig, Rep. Prog. Phys. **78**, 104501 (2015).
[10] I. Žutić, J. Fabian, and S. D. Sarma, Rev. Mod. Phys. **76**, 323 (2004).
[11] Ya. V. Fominov, A. A. Golubov, T. Yu. Karminskaya, M. Yu. Kupryanov, R. G. Deminov, and L. R. Tagirov, JETP Lett. **91**, 308 (2010).
[12] P. V. Leksin, N. N. Garif'yanov, J. Schumann, H. Vinzelberg, V. Kataev, R. Klingeler, O. G. Schimdt, and B. Büchner, Appl. Phys. Lett. **97**, 102505 (2010).
[13] T. Y. Karminskaya, A. A. Golubov, and M. Y. Kupriyanov, Phys. Rev. B **84**, 064531 (2011).
[14] C.-T. Wu, O. T. Valls, and K. Halterman, Phys. Rev. B **90**, 054523 (2014).
[15] J. Zhu, I. N. Krivorotov, K. Halterman, and O. T. Valls, Phys. Rev. Lett. **105**, 207002 (2010).
[16] A. I. Buzdin, Rev. Mod. Phys. **77**, 935 (2005).
[17] J. Bardeen, L. N. Cooper, and J. R. Schrieffer, Phys. Rev. **108**, 1175 (1957).
[18] A. I. Buzdin and M. Y. Kupriyanov, Pis'ma Zh. Eksp. Teor. Phys. **52**, 1089 (1990) [JETP Lett. **52**, 487 (1990)].
[19] K. Halterman and O. T. Valls, Phys. Rev. B **66**, 224516 (2002).
[20] E. A. Demler, G. B. Arnold, and M. R. Beasley, Phys. Rev. B **55**, 15174 (1997).
[21] F. S. Bergeret, A. F. Volkov, and K. B. Efetov, Phys. Rev. Lett. **86**, 3140 (2001); Phys. Rev. B **68**, 064513 (2003).
[22] K. Halterman, P. H. Barsic, and O. T. Valls, Phys. Rev. Lett. **99**, 127002 (2007).
[23] P. H. Barsic, O. T. Valls, and K. Halterman, Phys. Rev. B **75**, 104502 (2007).
[24] K. Halterman and O. T. Valls, Phys. Rev. B **80**, 104502 (2009).
[25] V. I. Zdravkov, J. Kehrle, G. Obermeier, D. Lenk, H.-A. K. von Nidda, C. Müller, M. Y. Kupriyanov, A. S. Sidorenko, S. Horn, R. Tidecks, and L.R. Tagirov, Phys. Rev. B **87**, 144507 (2013).
[26] V. L. Berezinskii, JETP Lett. **20**, 287 (1975).
[27] F. Chiodi *et al.*, Europhys. Lett. **101**, 37002 (2012).
[28] C. T. Wu, O. T. Valls, and K. Halterman, Phys. Rev. Lett. **108**, 117005 (2012).
[29] C. T. Wu, O. T. Valls, and K. Halterman, Phys. Rev. B **86**, 184517 (2012).
[30] Y. Gu, G. B. Halász, J. W. A. Robinson, and M. G. Blamire, Phys. Rev. Lett. **115**, 067201 (2015).
[31] F. S. Bergeret, A. F. Volkov, and K. B. Efetov, Rev. Mod. Phys. **77**, 1321 (2005).
[32] M. Eschrig and T. Löfwander, Nat. Phys. **4**, 138 (2008).
[33] P. V. Leksin, N. N. Garif'yanov, I. A. Garifullin, Ya. V. Fominov, J. Schumann, Y. Krupskaya, V. Kataev, O. G. Schmidt, and B. Büchner, Phys. Rev. Lett. **109**, 057005 (2012).
[34] F. S. Bergeret, A. F. Volkov, and K. B. Efetov, Appl. Phys. A **89**, 599 (2007).
[35] Y. Kalcheim, O. Millo, A. DiBernardo, A. Pal, and J. W. A. Robinson, Phys. Rev. B **92**, 060501(R) (2015).
[36] A. Singh, S. Voltan, K. Lahabi, and J. Aarts, Phys. Rev. X **5**, 021019 (2015).
[37] K. Halterman and M. Alidoust, Phys. Rev. B **94**, 064503 (2016).
[38] A. Fert, Rev. Mod. Phys. **80**, 1517 (2008).
[39] E. Moen and O. T. Valls, Phys. Rev. B **95**, 054503 (2017).
[40] A. F. Andreev, Sov. Phys. JETP **19**, 1228 (1964).
[41] J. Linder, T. Yokoyama, and A. Sudbø, Phys. Rev. B **79**, 224504 (2009).
[42] C. Visani, Z. Sefrioui, J. Tornos, C. Leon, J. Briatico, M. Bibes, A. Barthélémy, J. Santamaría, and J. E. Villegas, Nat. Phys. **8**, 539 (2012).

[43] Z. P. Niu, Europhys. Lett. **100**, 17012 (2012).
[44] Y.-Q. Ji, Z.-P. Niu, C.-D. Feng, and D.-Y. Xing, Chin. Phys. Lett. **25**, 691 (2008).
[45] G. E. Blonder, M. Tinkham, and T. M. Klapwijk, Phys. Rev. B **25**, 4515 (1982).
[46] S. Kashiwaya, Y. Tanaka, M. Koyanagi, and K. Kajimura, Phys. Rev. B **53**, 2667 (1996).
[47] M. J. M. de Jong and C. W. J. Beenakker, Phys. Rev. Lett. **74**, 1657 (1995).
[48] I. Žutić and O. T. Valls, Phys. Rev. B **61**, 1555 (2000).
[49] S. Takahashi and S. Maekawa, Phys. Rev. B **67**, 052409 (2003).
[50] A. A. Jara, C. Safranski, I. N. Krivorotov, C.-T. Wu, A. N. Malmi-Kakkada, O. T. Valls, and K. Halterman, Phys. Rev. B **89**, 184502 (2014).
[51] P. G. de Gennes, *Superconductivity of Metals and Alloys* (Addison-Wesley, Reading, MA, 1989).
[52] P. F. Bagwell, Phys. Rev. B **49**, 6841 (1994).
[53] F. Sols and J. Ferrer, Phys. Rev. B **49**, 15913 (1994).
[54] J. Sanchez-Canizares and F. Sols, Phys. Rev. B **55**, 531 (1997).
[55] C.-T. Wu, O. T. Valls, and K. Halterman, Phys. Rev. B **86**, 014523 (2012).